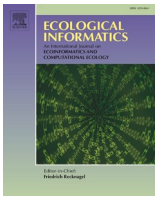
Ecological Informatics 84 (2024) 102846



Contents lists available at ScienceDirect

Ecological Informatics

journal homepage: www.elsevier.com/locate/ecolinf



Automatic pine wilt disease detection based on improved YOLOv8 UAV multispectral imagery

Shaoxiong Xu [a,b], Wenjiang Huang [a,b,*], Dacheng Wang [b], Biyao Zhang [b,f], Hong Sun [c], Jiayu Yan [c], Jianli Ding [a], Jinjie Wang [a], Qiuli Yang [a], Tiecheng Huang [a,b], Xu Ma [a], Longlong Zhao [d], Zhuoqun Du [e]

[a] College of Geography and Remote sensing Sciences, Xinjiang University, Urumqi 830046, China,
[b] Key Laboratory of Remote Sensing and Digital Earth, Aerospace Information Research Institute, Chinese Academy of Sciences, Beijing 100101, China
[c] Key Laboratory of National Forestry and Grassland Administration on Forest and Grassland Pest Monitoring and Warning, Center for Biological Disaster Prevention and Control of National Forestry and Grassland Administration, Shenyang 110034, China,
[d] Shenzhen Institutes of Advanced Technology, Chinese Academy of Sciences, Shenzhen 518055, China
[e] School of Economics and Management, Beijing Jiaotong University, Beijing 100044, China
[f] Key Laboratory of Earth Observation of Hainan Province, Hainan Aerospace Information Research Institute, Sanya 572029, China

ARTICLE INFO

Keywords:
Pine wilt disease (PWD)
Multispectral UAV imagery
Deep learning
YOLOv8

ABSTRACT

The pine wilt disease (PWD) can cause destructive death to pine trees in a short period. Utilizing unmanned aerial vehicle (UAV) remote sensing technology to promptly identify PWD-infected trees has become an effective and feasible method for precise PWD monitoring. In this study, UAV multispectral imagery was used to analyze the sensitive spectral bands and different vegetation indices for PWD discriminability. A dataset of optimal spectral combinations from visible light and multispectral images was constructed, along with an improved YOLOv8 deep learning model for rapid and accurate identification of PWD-infected trees. The improved YOLOv8 model used omni-dimensional dynamic convolution (ODConv) to enhance the performance of convolutional networks, designed a dynamic head (DyHead) module to capture PWD features more accurately, and applied MPDioU to improve the regression accuracy and model runtime efficiency. Experimental results showed that the mAP@0.5 of the improved YOLOv8 model increased to 89.1 %, with a user accuracy of 90 % and a recall rate of 93.1 %. This achieved rapid and accurate detection of PWD-infected trees, providing effective technical support for automatic identification of PWD epidemic areas and control of PWD outbreaks based on UAV multispectral imagery.

1. Introduction

Pine wilt disease (PWD) is a globally significant pine tree disease caused by the pine wood nematode (PWN). It poses a major threat to ecological safety, biological security, and economic development owing to its high infectivity, virulence, and rapid disease progression (Futai, 2013; Rutherford et al., 1990). PWD is transmitted by insects, such as Monochamus alternatus and Callidiellum rufipenne. When a pine tree is infected with PWD, its needles change color from deep green to red and the entire tree can die within 40 d. Pine forests can be destroyed within 3–5 years of infection (Park et al., 2013 Ye, 2019). Since its discovery in North America in 1905, PWD has caused significant economic losses and a decline in the global ecological service value (Kim et al., 2009; Lee et al., 2021). As global temperatures increase, more regions are threatened by PWD (Gruffudd et al., 2019). Currently, PWD management often relies on manual exploration, followed by the felling, burning, and fumigation of infected and dead trees, which is inefficient (Pu and Gong, 2019). Monitoring PWD-infected wood is crucial for disease prevention and control. Timely and effective detection of affected wood is vital for controlling the early spread of PWD, reducing monitoring and management costs, and mitigating damage, thereby enhancing forest protection in epidemic areas.

Numerous researchers have conducted extensive studies on PWD. In current studies on the detection of PWD-infected wood, ground-based observational experiments focusing on physiological changes in pine tree canopies are important. Iordache et al. studied spectral reflectance

* Corresponding author at: College of Geography and Remote sensing Sciences, Xinjiang University, Urumqi 830046, China.
E-mail address: huangwj@aircas.ac.cn (W. Huang).

https://doi.org/10.1016/j.ecoinf.2024.102846
Received 23 April 2024; Received in revised form 3 October 2024; Accepted 4 October 2024
Available online 23 October 2024
1574-9541/© 2024 The Authors. Published by Elsevier B.V. This is an open access article under the CC BY license (http://creativecommons.org/licenses/by/4.0/).

characteristics and confirmed significant differences between healthy and PWD-infected wood in the red (R) wavelength region (688 nm) (Iordache et al., 2020). This finding suggests that the early detection of infected trees can be achieved by monitoring spectral reflectance characteristics. Kim et al. analyzed 10 vegetation indices used for detecting PWD-infected wood using R and infrared (IR) wavelengths and found significant changes before and after PWD infection, such as variations in the normalized difference vegetation (NDVI) and enhanced vegetation (EVI) indices, reflecting changes in photosynthesis and chlorophyll content, thus providing an effective means for PWD detection (Kim et al., 2018). Xue et al. identified the spectral characteristics of affected wood by analyzing the spectral bands under different light conditions and growth environments (Xue et al., 2021). However, these methods also have limitations, such as interference from environmental factors (weather conditions and soil moisture) on spectral characteristics and vegetation indices and difficulty in detecting physiological changes during the early stages of PWD infection prior to needle discoloration.

Many research institutions and scholars have begun applying satellite remote sensing technology to monitor forest pests and diseases. Satellite remote sensing has been used in the United States of America (USA) to monitor the area and extent of damage to broadleaf forests infested by pests and diseases (Riley, 1989). Such as the use of satellite remote sensing in the United States (USA) to monitor the extent and distribution of pest infestations in broadleaf forests (Riley, 1989). Rencz and Nemeth (1985) used Landsat Multispectral Scanner data to monitor *lymantria dispar* and *dendroctonus ponderosae* in forests and analyzed the accuracy differences between various bands. In 1982, Japan began researching the application of USA resource satellites for monitoring forest pests and diseases. In China, the application of remote sensing technology to pest monitoring began relatively late. In the early 1990s, Yang et al. (2015) used TM images from the Anhui Province to monitor the winter generation of pine caterpillars (Dendrolimus sp.), producing distribution maps that distinguished between severe, light, unaffected, and non-forested areas. Wang et al. (2022a, 2022b) conducted in-depth research on TM image-monitoring technology for pine caterpillar disasters. However, the application of satellite remote sensing for PWD monitoring is limited by the spatial resolution of remote sensing images, atmospheric interference, and revisit cycles.

Drone aerial photography can rapidly obtain large-scale remote sensing images of pine forests, and when combined with deep learning algorithms for detecting diseased wood targets, it can rapidly identify the geographic coordinates of diseased wood, saving time for subsequent disposal (Liu et al., 2021). Therefore, the use of high-resolution remote sensing images from drones, combined with automatic recognition algorithms, is a primary method and a significant research direction for rapidly identifying suspected discolored wood due to PWD (Ye et al., 2022). Healthy pines have green needles, and diseased pines die from lack of water due to clogged petioles, and the color of the needles will gradually change from green to yellow or reddish brown. Healthy pine trees have green needles, while the needle color of diseased trees gradually changes from green to yellow or reddish-brown due to lack of water caused by clogged petioles (Istiak et al., 2023). Symptoms include reduced resin secretion, yellowing of needles that do not fall off, and eventual wilting and death, which typically develop during late summer to late autumn. Thus, changes in canopy color are key to identifying PWD infections (Vollenweider and Günthardt-Goerg, 2006; Abelleira et al., 2011; Eugenio et al., 2021). Based on the differences in appearance between diseased and healthy trees, researchers have proposed the use of drones equipped with visible light devices to identify PWD. For example, Tao et al. (2020) used fully convolutional neural networks (CNNs) to identify the pixels of infected wood in visible images, achieving a detection accuracy of >97 %. Apan et al. (2004), and Bochkovskiy et al. (2004) proposed a PWD-infected wood detector (MFTD) using multiband imaging fusion, achieving accuracies of 87.2, 93.5, and 84.8 % in the early, middle, and late stages of infection, respectively, revealing characteristics hidden within narrow spectral ranges and meeting the accuracy requirements for PWD-infected wood detection. However, detection is time consuming, costly, and has a low degree of automation. (Liu et al., 2022) used a relief feature selection algorithm combined with a Visual Geometry Group(VGG) network and an attention mechanism to achieve an average detection accuracy of 85.45 %. Ren et al. (2022) used a global multiscale channel adaptation network to detect PWD-infected wood and achieved average precision and recall rates of 79.8 and 86.6 %, respectively. Oide et al. (2022) improved PWD detection accuracy using an artificial neural network combined with Red, Green, Blue (RGB) and Hue, Saturation, Value (HSV) color space datasets.

However, visible-light images only contain information from the R, green (G), and blue (B) bands, which may pose challenges in PWD detection, such as high altitude and complex feature environments, potentially reducing detection accuracy and efficiency. Multispectral equipment can capture multispectral images, including additional spectral bands, such as G, R, near-infrared (NIR), and red-edge image information (Franke and Menz, 2007). Multispectral images divide spectral information into multiple spectral bands, allowing additional information to be obtained from many spectral channels and revealing characteristic features hidden within narrow spectral ranges, thereby meeting the accuracy requirements for PWD detection in complex ground environments (Zong and Bi, 2022). For example, Iordache et al. (2020) studied the spectral reflectance characteristics and confirmed that the R wavelength region (688 nm) showed the most significant differences between healthy and infected trees. Smith et al. (2021) investigated 10 vegetation indices used for PWD detection and found that the indices using R and IR wavelengths showed significant changes before and after pine tree infection.

Therefore, the use of multispectral and hyperspectral equipment to collect spectral information for PWD identification has gradually increased. For example, Awad (2018) used the traditional random forest classification algorithm combined with multispectral or hyperspectral images to achieve classification accuracies >91 % for PWD-infected wood. Qin et al. (2023) proposed a neural network algorithm based on ScanNet using drone multispectral images and achieved an overall accuracy of 79 %. Park et al. (2021) generated vegetation indices from multispectral data by combining visible light images to train a deep learning model, achieving an mAP@0.5 of 86.63 % for detecting suspected PWD-infected wood. However, the detection accuracy still requires improvement, and the robustness of the model was relatively poor.

To further advance PWD-infected wood identification technology, this study explored improved versions of deep learning models, including Faster R-CNN, YOLOv7, and YOLOv8. These models have shown significant improvements in speed, accuracy, and robustness, making them particularly suitable for detecting infected wood in complex environments and at various stages. Faster R-CNN, a classic deep learning object detection framework, efficiently locates regions of interest in images using its regional proposal network and a rapid Region of Interest (ROI) alignment method (Ren et al., 2015). To adapt it for PWD-infected wood detection, an improved feature pyramid network and balanced positive–negative sample ratio strategy can be introduced to enhance the model localization capability and recognition accuracy in complex backgrounds. YOLOv7, an efficient version of the YOLO series, enhances small-object detection capability through an improved path aggregation network and deeper residual structures. YOLOv7 can optimize the detection process for PWD-infected wood by introducing adaptive anchor sizes and automatically adjusted thresholds, making the model more suitable for detecting infected wood of different sizes and shapes (Wang et al., 2022a, 2022b). YOLOv8's primary features include a more advanced convolutional architecture and attention mechanism, which improve the speed and robustness in complex environments (Doe et al., 2023; de Melo Lima et al., 2024; Deng et al., 2024; Rani et al., 2024; Zhou et al., 2024;). For PWD-infected wood identification, YOLOv8 can combine hyperspectral data and use advanced multiscale

detection strategies to significantly improve detection accuracy and efficiency.

In summary, most existing studies rely on visible light images for identification. The recognition methods using single visible light or multispectral images are inevitably affected by the phenomena of "same object, different spectra" and "different objects, same spectrum," leading to a variety of misdetections and omissions, thereby affecting recognition accuracy. In addition, basic deep learning models may overfit training data, resulting in poor performance on new and unseen data and limited generalization ability when faced with new tasks that differ from the training data distribution. This study proposes a method based on a combination of visible light and multispectral imaging bands using an improved YOLOv8 deep learning object detection algorithm with a multi-channel dataset. The algorithm designs a C2f-omni-dimensional dynamic convolution (ODConv) module to replace the basic C2f module in YOLOv8, incorporating a dynamic convolution method to align the sampling of the model with the shape and size of the target. The attention mechanism dynamic head (DyHead) module was added to replace the basic Detect module in YOLOv8 and to incorporate a residual network, expanding the model's receptive field thereby improving the network learning ability. In addition, the MPDioU loss function algorithm combines a non-monotonic focusing mechanism with bounding box geometric factors to enhance the quality of the bounding box and thus more accurately identify the distribution of PWD-infected wood. These approaches provide scientific support for rapid and accurate intelligent identification of PWD-infected wood.

The primary contributions of this study are as follows:

1. Experiments were conducted using field-collected data to compare the characteristic differences between healthy and PWD-infected trees in multispectral bands and to screen the most suitable vegetation indices for PWD detection.
2. Experiments were conducted using a combination of multispectral and visible light images, and ablation experiments were performed.
3. An improved YOLOv8 model was proposed to improve the accuracy of PWD-infected tree identification.
4. The improved YOLOv8 model was used for a comparative study of band-channel combinations to improve PWD tree detection accuracy. Detection results were compared based on the use of visible light, multispectral images, and vegetation indices. Experiments showed that using RGB, NIR, red-edge, and normalized difference red-edge (NDRE) indices improved PWD tree-detection accuracy.

2. Materials and methods

2.1. Study area

The experimental area is located near Dahua Fang Reservoir in Dongzhou District, Fushun City, Liaoning Province, China (124°1–124°24′E, and 42°0–41°16′N), with an approximate area of 1 km^2 (Fig. 1). This area has a temperate continental monsoon climate, with an average annual temperature of 13.9 °C and an average annual precipitation of 826.8 mm. The primary tree species are Korean and Chinese pines, ranging from 10 to 20 years in age. PWD is the primary disease in this forested area and typically occurs from May to October each year.

2.2. Non-imaging hyperspectral sensor data collection and processing

Orthophoto imagery from an UAV was used as the experimental sampling area. The coordinates of dead PWD-infected trees were obtained by combining global positioning system(GPS) and real-time kinematic (RTK)measurements. A sample survey of PWD-infected trees is presented in Table 1.

The experiment was conducted on July 6, 2023. Fifteen pine trees, including visually identifiable healthy, suspected withered, and withered trees, were selected for needle sampling. To ensure needle integrity and minimize moisture loss, the needles were harvested with their sheaths. They were sealed in bags and transported to the laboratory for processing. Needles were divided into three groups: healthy, suspected withered, and withered (Park et al., 2013). Each group comprised 400 needles. The suspected withered needle group consisted of 200 healthy combined with 200 withered needles. Spectral measurements of the pine needles were conducted using an analytical spectral device (ASD) FieldSpec 4 HR NG portable spectrometer in a dark room.

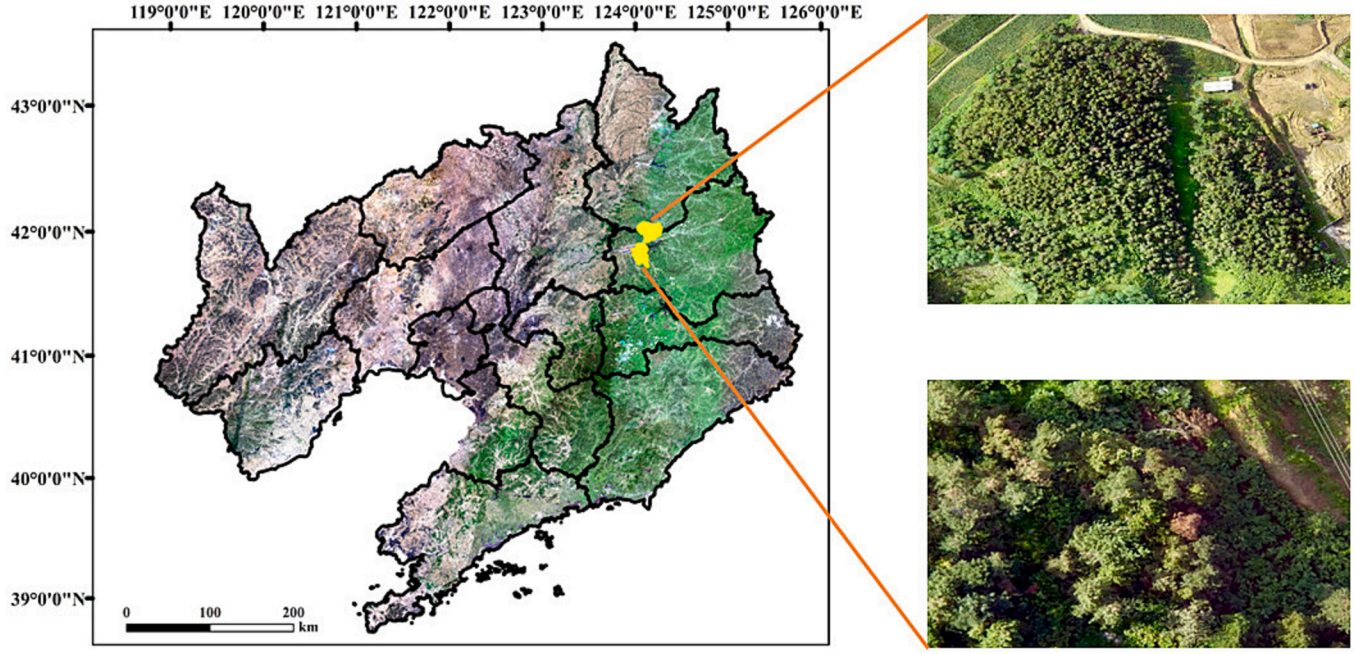


Fig. 1. Location and snapshots of the research area.

Table 1
Record of sample site investigation.

Number	Tree Height (m)	Crown diameter (m)	Notes	Number	Tree Height (m)	Crown diameter (m)	Notes
1	10.6	6.5	SW	9	9.33	4	H
2	12.76	4.87	SW	10	9.67	6.12	W
3	9.88	7.24	H	11	8.36	5	SW
4	10.61	4.7	W	12	8.9	3.8	SW
5	10.6	7.8	SW	13	8.67	6	W
6	8.24	8.1	H	14	6.63	3.3	W
7	7.13	5.5	W	15	13,8	4.1	SW

Note: SW, W, and H represent suspected withered, withered, and healthy pines, respectively.

2.3. Drone data collection and processing

The images were captured on July 6, and August 25, 2023, using a DJI M300 equipped with a multispectral camera (Long Guang Yuchen MS600 Pro, Beijing, China). This study used drone multispectral data that included sensitive bands for PWN-infected trees, identified using a non-imaging hyperspectral sensor. The multispectral camera included bands for R, G, B, NIR, and red-edge 720 and 750 nm. The UAV flight parameters are shown in Table 2. To obtain the necessary data for this study, we conducted multiple drone flights, ultimately acquiring 3500 visible images and 1000 multispectral images.

For calibrated UAV multispectral images, a sharpening filter was applied to enhance the feature points of the objects in the images. The 940 stitched images were divided into a dataset in a ratio of 8:1:1 for training, validation, and testing. Subsequently, data augmentation was performed on the training set. To enhance the robustness and generalization ability of the model and avoid overfitting; rotations, flips, mixing, and scaling were applied to the initial 750 training images, resulting in 6050 images. In this study, the diameter of the tree canopy in the drone imagery was $<600 \times 600$ pixels. Therefore, the existing 1280×960-pixel images were cropped from the center to 600×600 pixels. The dataset was manually checked to remove images that did not meet the requirements, such as those with overly complex backgrounds or interfering factors that affected the recognition of the primary object. Images with over- or under-exposure that lost image details were also removed. In addition, identical or almost identical images that were repeated multiple times, causing dataset bias and affecting the generalization ability of the model, were excluded. After pre-processing, 17,314 images were obtained, of which 8560 were used for training, 1070 for validation, and 985 for testing.

The dataset was annotated using an open-source labeling annotation tool. Several rectangular boxes were drawn in the images to delineate the boundaries of pine tree crowns infected with PWD, with each box containing a single PWD-infected tree crown. UAV multispectral images processed using different feature extraction methods maintained consistent tree-crown positions. Annotation files created based on various band feature methods and vegetation indices selected for the red-edge band can also be used to annotate PWD-infected trees in other datasets. Observations from this experiment revealed that PWD had a relatively prolonged duration in the region, with instances of partial discoloration in which half of a single PWD-infected tree crown appeared dead, whereas the other half remained healthy, as depicted in Fig. 2. Only two types of discoloration were observed: suspected withered (SW) and withered (W) pines. To better differentiate between the discoloration types of PWD-infected trees, annotations were made for three categories: visually identifiable healthy (H), suspected withered (SW), and withered (W) trees. The annotated rectangular boxes (X_{min}, X_{max}, Y_{min}, and Y_{max}) and the corresponding category information were saved as .txt files, forming a YOLO-format dataset.

Table 2
Drone usage parameters.

Flight parameters	Visible light images	Multispectral images
Ground Sampling Distance (m)	150	100
Flight speed (m/s)	15	10
Forward overlap ratio (%)	80	85
Side overlap ratio (%)	80	85
Capture interval (s)	8	5

The R, NIR, red-edge 720 and 750 nm bands of multispectral UAV imagery exhibited significant differences between PWD-infected trees with varying degrees of discoloration and healthy trees. Two vegetation indices, NDVI and NDRE, also showed notable variation among these trees. By selecting these bands and indices as feature bands, multispectral UAV imaging may offer a more accurate identification of PWD-infected trees than visible-light UAV imaging. Constructing a dataset for detection models using these features is expected to enhance the detection performance. The dataset compositions combining the visible light, NIR, red-edge, NDVI, and NDRE images for training are listed in Table 3.

2.4. Technical flowchart

Based on the data acquired from PWD-infected trees combined with multispectral UAV remote sensing spectral information, sensitive bands for identifying PWD-infected trees and vegetation indices indicative of PWD-infected tree distinguishability were selected. Visible light, NIR, red-edge, NDVI, and NDRE images were combined to train classic deep learning networks, including the Faster R-CNN, YOLOv8, and YOLOv7. Based on the precision and runtime of the different model training results, improvements were made to the YOLOv8 model modules to construct a more accurate deep learning model for automatic PWD-infected tree identification. This process aimed to provide technical support for rapid large-scale monitoring. The technical roadmap is shown in Fig. 3.

2.5. Method for extracting features of PWD-infected trees from multispectral UAV images

2.5.1. Euclidean distance

This study employed the Euclidean distance formula (1) to quantitatively evaluate the ability of multispectral UAV imagery of different bands to identify discolored PWD-infected trees. If there is a significant change in the spectral curve within a certain band range, creating spectral differences between healthy and PWD-infected pine trees, the band range can be considered a sensitive band for identifying dead PWD-infected trees. Distance analysis was used to assess the magnitude of the differences between the observed values in each experimental group. The larger the relative distance, the greater is the data difference, whereas the smaller the relative distance, the smaller is the data difference (Yahyanejad et al., 2011; Yu et al., 2021).

$$D = \sqrt{\sum_{k=1}^{n} (x_k - y_k)^2} \quad (1)$$

2.5.2. J-M distance

In the field of remote sensing, the J-M distance is commonly used to

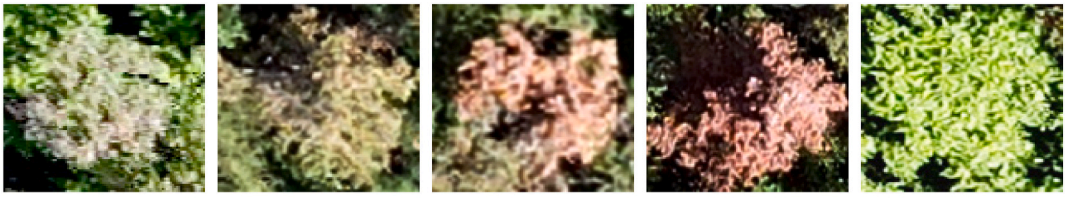


Fig. 2. Trees with different degrees of discoloration due to pine wilt disease (PWD) and healthy pine trees; (a) ands (b) suspected withered trees, (c) and (d) withered trees, and (e) healthy pine tree.

Table 3
Dataset band combinations.

Dataset	Band combination	Data description
Dataset 1	RGB	Composed of R, G, and B bands.
Dataset 2	Original reflectance group	Composed of R, G, B, REI, REII, and NIR bands.
Dataset 3	NDRE group	Composed of G, R, B, NIR, REI, REII, and NDRE bands.
Dataset 4	NDVI group	Composed of R, G, B, REI, REII, NIR, and NDVI bands.

Note: REI and REII represent suspected and withered pines, respectively.

indicate the separability of land-cover categories, and is a measure of separability based on conditional probability density. In this study, the J-M distance was used to evaluate 30 spectral indices to distinguish between healthy and PWD-infected pine trees. The J-M distance ranges from 0 to 2. A J-M distance $\leq$1.0 indicates that there is no spectral separability between the categories to be classified and 1.0 < J-M distance <1.9 indicates that there is some degree of spectral separability between the categories to be classified. A J-M distance $\geq$1.9 indicates that there is good spectral separability between the categories to be classified (Ma et al., 2010).

2.6. Multispectral UAV imagery for deep learning-based individual PWD recognition

2.6.1. Improved YOLOv8 algorithm model architecture

The YOLOv8 network architecture can be divided into four sections: input, backbone, neck, and head (Fig. 4).

To address the issues of high rates of missed detections or false positives, inaccurate object localization, and the inability to accurately identify targets in UAV multispectral image detection models based on the YOLOv8 baseline and Faster R-CNN, improvements have been made to the YOLOv8 algorithm (Ge et al., 2021). These improvements are as follows.

(1) ODConv Module Principles

The ODConv module is designed to replace the C2f module in the YOLOv8 baseline, incorporating dynamic convolutional methods to ensure that model sampling aligns more closely with the shapes and sizes of the targets. ODConv is a dynamic convolutional method that focuses on dynamism across dimensions, such as spatial, input, and output channels. It linearly weights multiple convolutional kernels, providing dynamic convolutional input dependency (Lou et al., 2023). During the dynamic convolutional process, the weights of the convolutional kernels were not fixed but were dynamically adjusted based on the input data. This allows the kernels to adapt better to the features of the input data, thereby enhancing the performance of the convolutional network (Li et al., 2022).

(2) DyHead Module Principles

The DyHead module was introduced by adding an attention mechanism to replace the Detect module in the YOLOv8 baseline and integrating it with a residual network to expand the model's receptive field and enhance its learning ability. GEM_YOLO uses a Dy-Head module based on attention mechanisms and unified objectives to capture targets more accurately (Dai et al., 2021). DyHead incorporates multiple self-attention mechanisms that comprehensively consider information from feature hierarchies, spatial positions, and task-aware output channels, thereby achieving a multifaceted fusion of scale, spatial, and task relatedness. DyHead comprises three key attention modules: scale, spatial, and task perception (Dai et al., 2021).

(3) MPDioU Loss Function Principles

The MPDioU loss function algorithm combines a nonmonotonic focusing mechanism with the geometric factors of the bounding boxes to improve their quality. During the training phase, the model optimization objective is to make each predicted box $B_{prd} = [x_{prd}, y_{prd}, w_{prd}, h_{prd}]^T$ and annotated box $B_{gt} = [x_{gt}, y_{gt}, w_{gt}, h_{gt}]^T$ as close as possible. In this study, the MPDioU loss function is defined based on Formula (2):

$$L_{MPDIoU} = 1 - MPDIoU \tag{2}$$

According to Fig. 5, all relevant factors of the existing bounding box regression loss functions can be derived from the LMPDIoU calculation factors proposed in this study. The proposed *MPDIoU* includes the relevant factors of existing bounding box regression metrics and simplifies the calculation process. Here, |C| represents the minimum enclosing rectangle area covering Bgtand Bprd; (x_c^{gt}, y_c^{gt}) and (x_c^{prd}, y_c^{prd}) denote the center coordinates of the ground truth and predicted boxes, respectively' w_{gt} and h_{gt} represent the width and height of the ground truth box, respectively; and w_{prd} and h_{prd} represent the width and height of the predicted box, respectively (Rohit et al., 2024).

An analysis based on Fig. 6 reveals that when two prediction and ground truth boxes have the same aspect ratio and their center points coincide but their width and height values differ, the prediction box inside the ground truth box has a higher MPDioU value than the prediction box outside the ground truth box. By contrast, the existing intersection over union (IoU) metrics yield the same values. This indicates that the bounding-box regression process of MPDioU tends to predict results with lower redundancy, leading to higher regression accuracy and efficiency.

2.6.2. Evaluation metrics

In the YOLOv8 model semantic segmentation, the IoU was used to evaluate model performance to determine key metrics, such as precision and recall. The IoU spans [0,1], where an IoU value >0.5 indicates a high degree of overlap between the predicted and ground truth boxes, thus indicating a higher accuracy of the detection algorithm, which can more accurately reflect the degree of overlap between the detection box and the actual target, making it particularly suitable for object localization tasks (Sunil et al., 2024). The computation is expressed by Eq. (3):

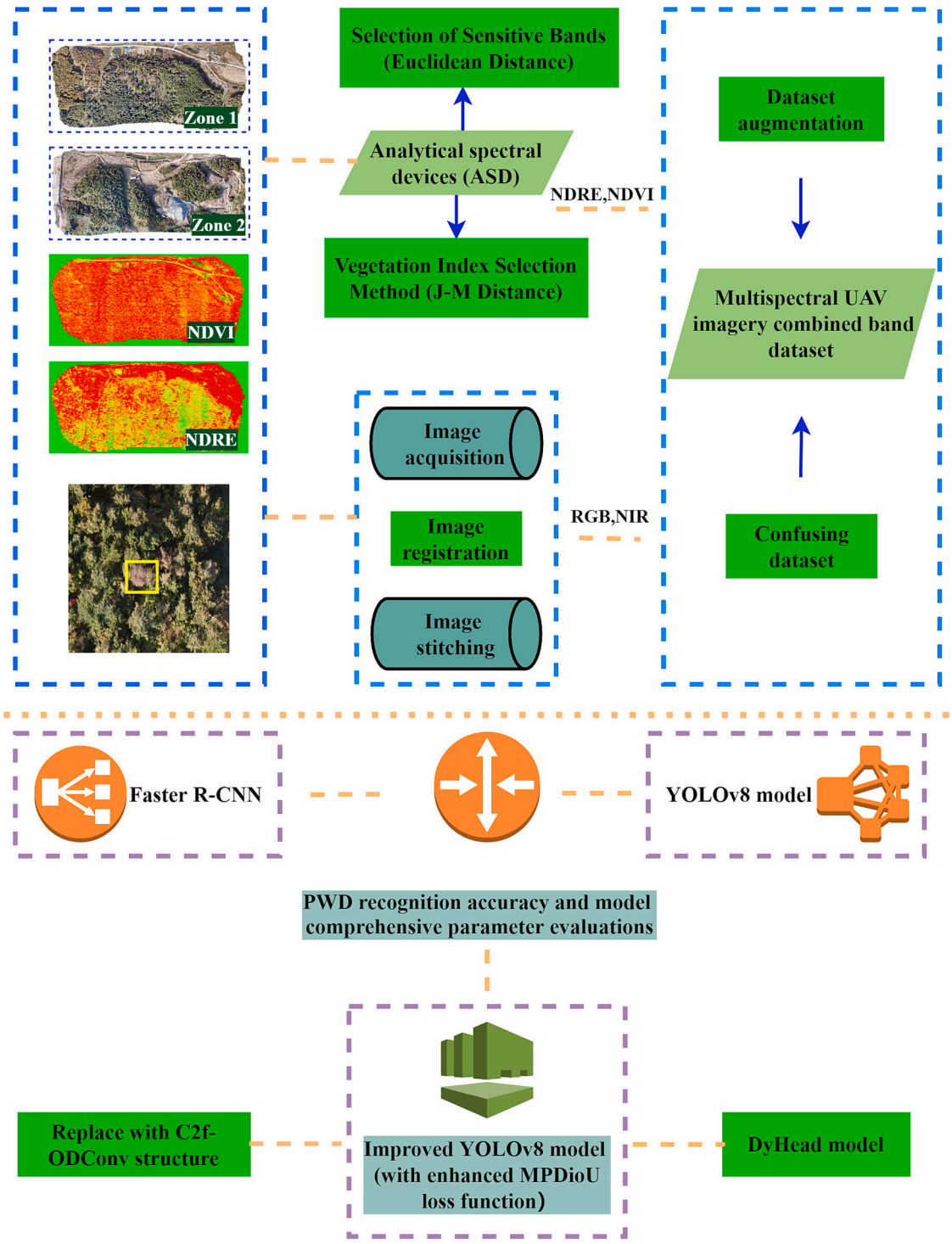


Fig. 3. Technical flowchart.

$$Iou = \frac{P \cup G}{P \cap G} \tag{3}$$

In Eq. (3), P refers to the model prediction, G refers to the manually annotated region, P∪G refers to the union area of P and G, and P∩G refers to the intersection area of P and G. This principle is illustrated in Fig. 7.

The evaluation metrics included accuracy(4), precision(5), recall(6), and mean average precision (mAP@0.5)(7), which were used to assess model performance. Precision refers to the ratio of true-positive predictions to the total number of predicted positives, which represents the classification accuracy of the network. The precision metric reflects the classification ability of the model, and is crucial for reducing false-positive predictions. High precision indicates that model predictions of negative examples are reliable. However, the recall is the ratio of correctly predicted true-positives to the actual total number of positives. This measures the ability of the model to identify all the positive cases. A high recall implies that the model effectively captures most of the targets, which is critical in real-world applications to reduce missed detections (Xiao et al., 2024).

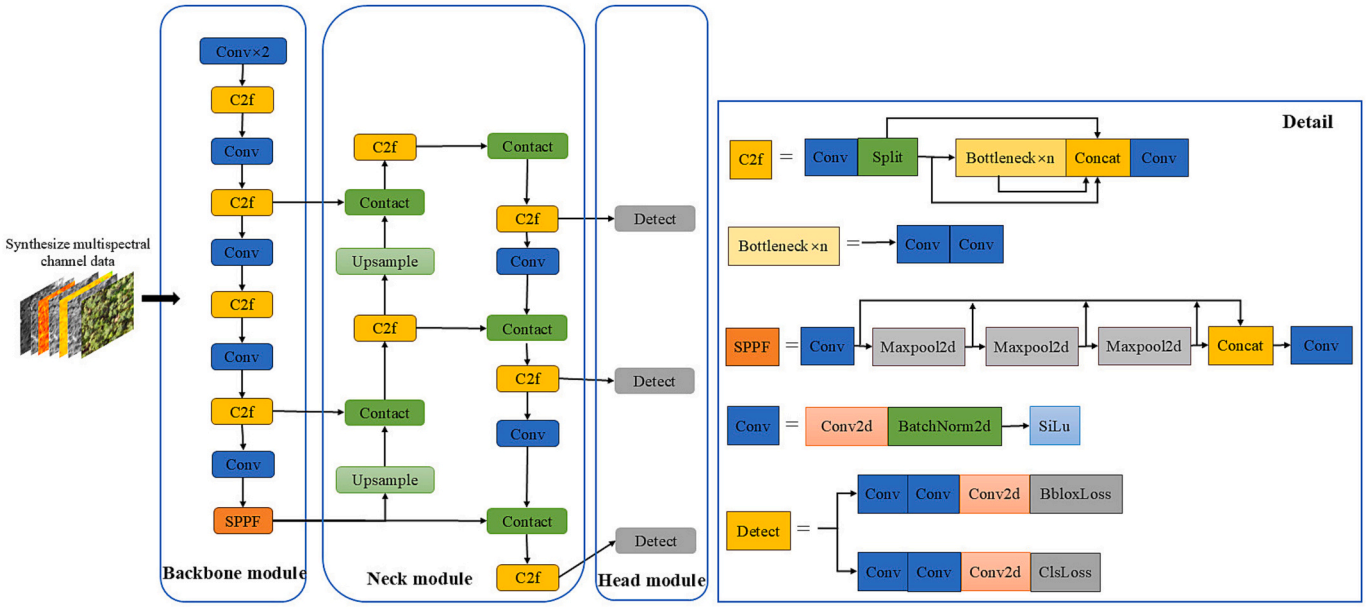


Fig. 4. Improved YOLOv8 network architecture.

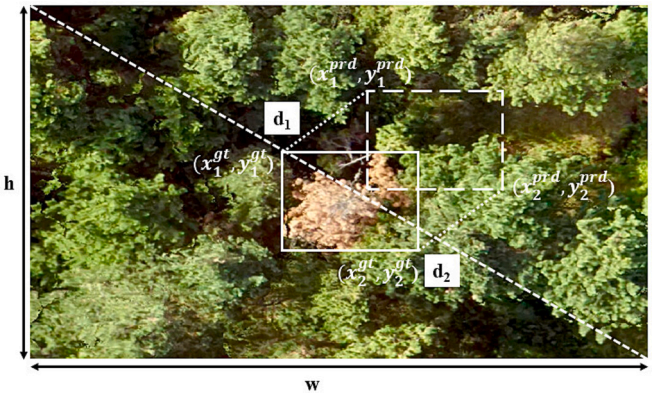


Fig. 5. Factors for computing LMPDIoU proposed in this study.

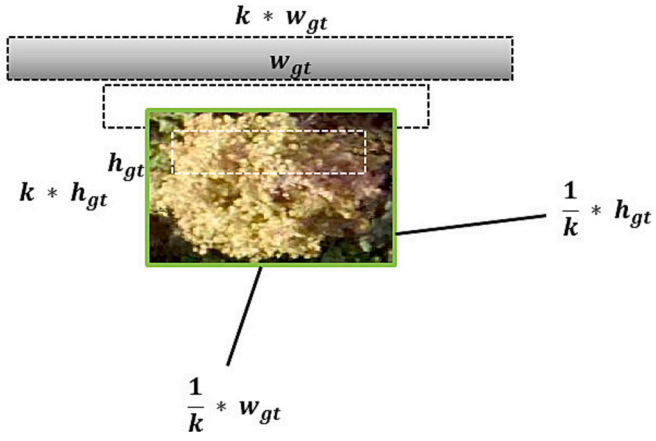


Fig. 6. Examples of predicted and annotated boxes with the same aspect ratio but different width and height values, where k > 1 and k∈ R. Solid lines represent annotated boxes, and dashed lines represent predicted boxes.



Fig. 7. Intersection over union principle diagram.

$$Accuracy = \frac{TP + TN}{TP + TN + FP + FN} \tag{4}$$

$$Precision = \frac{TP}{TP + FP} \tag{5}$$

$$Recall = \frac{TP}{TP + FN} \tag{6}$$

$$mAP = \frac{1}{N}\sum_{i=1}^{N} AP_i \tag{7}$$

In classification tasks, the actual results are categorized as true (positive) or false (negative), and the model predictions are also labeled as positive or negative. TP (true positives) and FP (false positives) represent the numbers of correctly and incorrectly predicted positive samples, respectively. FN (false negatives) indicates the number of incorrectly predicted negative samples, and N represents the number of data categories. The classification of positive and negative samples was determined using the intersection threshold between the predicted and actual regions. If both regions exceeded a certain threshold, the sample

was classified as positive; otherwise, as negative.mAP@0.5, which refers to the mean average precision when the IoU threshold is set at 0.5 for all categories. The mAP integrates both precision and recall, providing a comprehensive evaluation of model performance across all categories. This makes the mAP a widely used and insightful metric, particularly in multiclass detection tasks, where it offers a clear reflection of a model's overall performance (Zhenzuo et al., 2024). By combining these evaluation metrics, the performance of the model can be assessed from various perspectives.

3. Results and discussion

This section presents a quantitative analysis of the spectral characteristics and physiological vegetation parameters of PWD-infected trees, revealing distinct changes in pine trees affected by PWD. A comparative analysis of the spectral information of various land-cover types demonstrated differences between the spectral characteristics of PWD-infected trees and those of other land-cover types. This confirms the feasibility of using UAV multispectral imagery to identify PWD-infected trees.

3.1. Feature extraction of PWD-infected trees in UAV multispectral imagery

(1) Analysis of Spectral Characteristics and Physiological Vegetation Parameters

R_H, R_{SW}, and R_w represent the reflectance of healthy, suspected withered, and withered pine needles, respectively. As shown in Fig. 8, the spectral curve of the healthy pine needles exhibited the first peak at approximately 550 nm, followed by a gradual decrease in reflectance. At a wavelength of approximately 700 nm, the reflectance reached its lowest point and then gradually increased. Combined with Fig. 9, the physiological parameters of the vegetation were measured experimentally. The observed pattern of needle reflectance may be attributed to the fact that in the wavelength range of 400–700 nm, the spectral reflectance of plants was greatly influenced by chlorophyll. This spectral characteristic is generally consistent with the spectral changes extracted from the UAV multispectral imagery. Based on the analysis shown in Fig. 10, there were distinct differences in reflectance between the different types of pine needles and other land-cover types in terms of spectral characteristics. Therefore, it is feasible to use the measurement

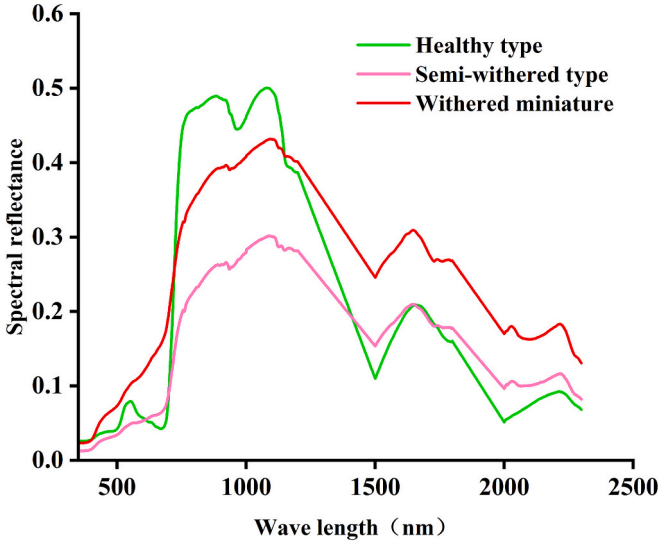


Fig. 8. Spectral curves of pine needles at different degrees of discoloration and withering compared to healthy pine needles.

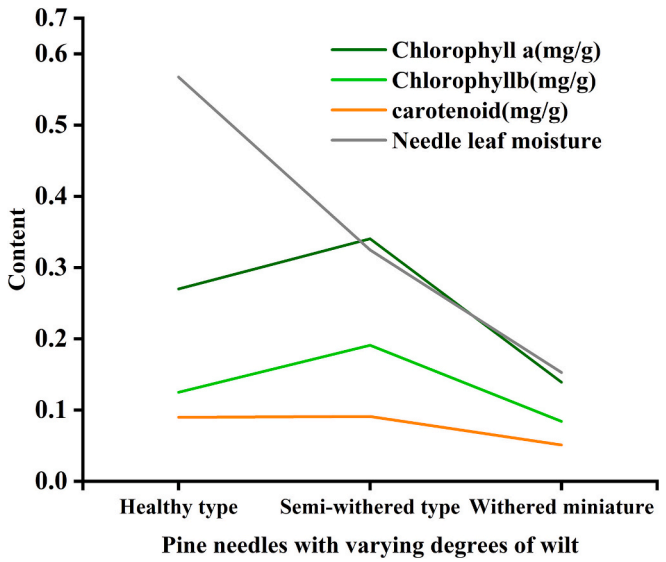


Fig. 9. Physiological parameter changes in pine needles at different degrees of complete discoloration and withering.

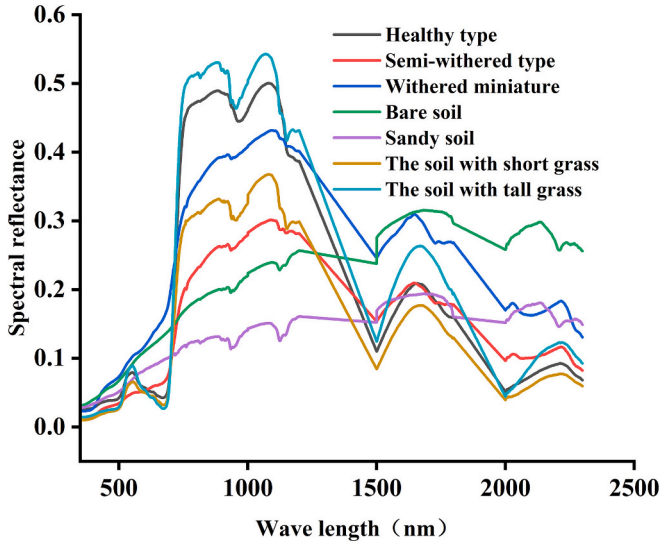


Fig. 10. Differently discolored dead pine needles and spectral curves of different types of ground cover.

method employed in this study to simulate the spectral characteristics of pine canopy layers in UAV multispectral imagery.

By comparing the sizes of the reflectance curves of the three lines in Fig. 10, it can be observed that in the wavelength range of 400–700 nm, $R_H < R_{SW} < R_W$; in the range of 700–1300 nm, $R_H > R_W > R_{SW}$; and in the wavelength range of 1300–2500 nm, $R_H < R_{SW} < R_W$. As shown in Fig. 11, using the spectral curves and first-order differentials of reflectance of the three groups of pine needle samples as basic data, the spectral characteristics during pine tree color change and withering were analyzed. During the transition from healthy to withered and withering pine needles, the chlorophyll content of the needles decreased gradually, resulting in a gradual increase in reflectance. In the wavelength range of 700–1300 nm, at approximately 700 nm, the reflectance of needle leaves began to increase sharply, indicating the appearance of the "red-edge" phenomenon in vegetation spectral characteristics. In the wavelength range of 1300–2500 nm, the spectral reflectance of vegetation is related to the leaf water content, with a decrease in the water content of pine needles leading to a significant increase in reflectance.

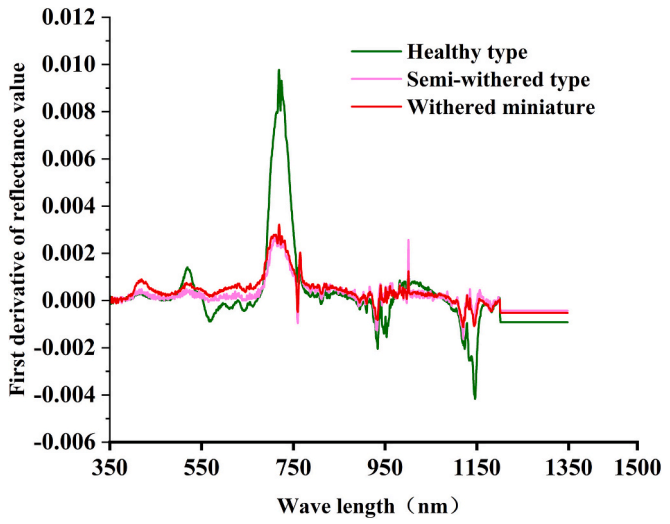


Fig. 11. First-order derivative of reflectance spectra for pine needles at different degrees of discoloration and withering compared to healthy pine needles.

(2) Feature Extraction Analysis of Sensitive Bands and Vegetation Index Discriminability

The spectral range of the data (MS600) included the following bands: 450 nm - B, 555 nm - G, 660 nm - R, 720 nm – red-edge I, 750 nm – red-edge II, and 840 nm - NIR. A quantitative analysis of the variations in the three curves within each band range was conducted, with the spectral curve of healthy pine needles as the reference. The relative distances between the spectral curves of pine needles with two different degrees of discoloration and withering and the spectral curve of healthy pine needles were calculated using the Euclidean distance formula. The results are summarized in Table 4. To differentiate between healthy pine needles and those with two different degrees of discoloration and withering, the red-edge band II was found to be the most sensitive, followed by the NIR, red-edge I, G and R bands. B was the least sensitive band.

In this study, the separability of healthy pine needles from those with different degrees of discoloration and withering was calculated using 30 spectral indices. Spectral indices were computed based on the spectral data of healthy pine needles, and the separability of those with different degrees of withering was assessed using the J-M distance formula. The results are summarized in Table 5 below.

According to Table 5, the J-M distances calculated for healthy pine needles and those with different degrees of discoloration and withering using the R_{gre}-R_{blue} spectral index were 0.93 and 1.0, respectively. This indicates that there is no spectral separability between healthy and withered pine needles. Thus, this index is not suitable for identifying suspected withered and withered pine trees. For the spectral indices $R_{blue}/R_{nir} + R_{gre}$ and $R_{blue}/R_{nir} + R_{red}$, the J-M distances calculated for healthy and withered tree pine needles were 1.75 and 1.02, respectively.

Table 4
The Euclidean distance of spectral curves of color changing withered and healthy pine needles.

Different wilting pine needles	Blue band (450 nm)	Green band (555 nm)	Red band (660 nm)	Red-edge band I (720 nm)	Red-edge band II (750 nm)	Near infrared band (840 nm)
$D_{suspected-withered}$	**0.95**	**2.94**	**1.84**	**10.18**	**24.03**	**23.39**
$D_{withered}$	**2.1**	**2.43**	**0.99**	**10.65**	**12.25**	**10.68**

Table 5
Hyperspectral characteristic parameters and spectral index.

Number	Spectral index	Formula	Reference	$J_{healthy\text{-}semi\ wilting}$	$J_{healthy\text{-}wilting}$
1	Differential vegetation index	$R_{nir} - R_{red}$	Jordan, 1969	1.85	1.8
2		$R_{red} - R_{gre}$	Xue and Su, 2017	1.7	1.65
3		$R_{gre} - R_{blue}$	Xue and Su, 2017	0.93	1.0
4		$R_{nir} - R_{gre}$	Xue and Su, 2017	2.00	2.00
5		$R_{blue} - R_{nir}$	Xue and Su, 2017	0.93	1.08
6		$R_{blue} - R_{red}$	Xue and Su, 2017	0.95	1.32
7	Ratio vegetation index	R_{red} / R_{gre}	Tian, 1998	2.00	2.00
8		R_{blue} / R_{nir}	Verrelst et al., 2008	0.52	1.05
9		R_{red} / R_{nir}	Pearson, 1972	1.97	2.00
10		R_{gre} / R_{nir}	Verrelst et al., 2008	2.00	2.00
11		R_{blue} / R_{red}	Pearson, 1972	0.57	1.32
12		R_{blue} /R_{gre}	Tang et al., 2003	1.43	0.97
13		$R_{blue} / R_{nir} + R_{gre}$	Tang et al., 2003	0.45	1.02
14		$R_{nir} / R_{nir} + R_{gre}$	Tang et al., 2003	1.75	1.02
15		$R_{gre} / R_{gre} + R_{nir}$	Zeng et al., 2022	2.00	2.00
16		$R_{red} / R_{gre} + R_{nir}$	Zeng et al., 2022	2.00	2.00
17		$R_{nir} / R_{red} + R_{gre}$	Wang et al., 2012	2.00	2.00
18		$R_{blue} / R_{red} + R_{gre}$	Zhang et al., 2023	1.25	1.77
19		$R_{gre} / R_{red} + R_{gre}$	Zhang et al., 2023	1.32	0.87
20		$R_{red} / R_{red} + R_{gre}$	Zhang et al., 2023	2.00	2.00
21		$R_{gre} / R_{nir} + R_{red}$	Zhang et al., 2023	2.00	2.00
22		$R_{blue} / R_{nir} + R_{gre}$	Zhang et al., 2023	0.45	1.75
23		$R_{red} - R_{blue} / R_{red} + R_{blue}$	Li et al., 2023	1.45	1.31
24		$R_{nir} - R_{blue} / R_{nir} + R_{blue}$	Aoden et al., 2023; Gitelson et al., 1996	1.05	1.36
25	Normalized differential vegetation index	$R_{nir} - R_{gre} / R_{nir} + R_{gre}$	Liu et al., 2020	1.48	1.26
26		$R_{nir} - R_{red} / R_{nir} + R_{red}$	Liu et al., 2020	2.00	2.00
27		$R_{gre} - R_{red} / R_{gre} + R_{red}$	Liu et al., 2020	2.00	2.00
28	Red vegetation index(NGRDI)	R_{red}-R_{gre} / $R_{red} + R_{red}$	Dong et al., 2020a, 2020b	2.00	2.00
29	Normalized differential red-edge vegetation index (NDRE)	$(R_{NIR} - R_{Red\ edge}) / (R_{NIR} + R_{Red\ edge})$	Han et al., 2021	2.00	2.00
30	Red-edge Chlorophyll vegetation index (RECl)	$(R_{NIR} / R_{Red\ edge}) - 1$	Ye et al., 2022	2.00	2.00

This indicates that although there is some spectral separability between healthy and withered pine needles, there is a significant overlap, making these indices unsuitable for identifying suspected withered trees. Similarly, both the R_{blue}/R_{gre} and $(R_{blue} - R_{gre})/(R_{gre} + R_{blue})$ spectral indices

were not suitable for identifying completely discolored and withered pine trees, and the $R_{blue}/R_{red} + R_{gre}$ spectral index was not suitable for identifying suspected withered trees. Spectral indices with J-M distances <1.90 revealed that using spectral indices constructed with the B band had little effect on identifying withered trees. When constructing vegetation indices using the G band, it is not advisable to use them simultaneously with the B band. In addition to the 12 spectral indices involving blue light mentioned above, the J-M distances calculated for the remaining 16 spectral indices for healthy and suspected withered pine tree needles, including healthy and withered pine needles, were all >1.90, indicating good spectral separability, which is consistent with the findings of recent studies by Kim et al. (2018) and Iordache et al. (2020). Given that hyperspectral imaging provides more detailed spectral information, it may offer higher accuracy in extracting the characteristics of trees infected with PWD. Future research should explore the potential of hyperspectral imaging in detecting PWD-infected trees.

3.2. Experimental environment and evaluation metrics analysis

This section provides a comparative analysis of the Faster R-CNN, YOLOv7, YOLOv8 basic, and improved YOLOv8 detection algorithms. It was observed that using the multichannel fusion Dataset 4 (NDRE group) significantly enhanced detection performance. Table 6 presents a performance comparison of the trained models for the four datasets. Based on the experiments conducted with the four models, model detection precision (precision) on Dataset 4 was observed to be the highest at 0.9, with a maximum recall rate (recall) of 0.931 and an mAP@0.5 of 0.891. This demonstrates that multispectral images from UAVs provide a more accurate identification of PWD-diseased trees than UAV visible-light images, and the improved YOLOv8 model performed the best among the tested models. Throughout all experiments, the improved YOLOv8 model exhibited the highest detection precision (precision) of 0.91 and a maximum recall rate (recall) of 0.931 on Dataset 4, thus validating the effectiveness of the improved model.

Using Dataset 4, the ablation experiments were conducted using the improved YOLOv8 model. The YOLOv8 basic model is denoted as M1; M2 incorporates the ODConv module with the M1; M3 applies the DyHead module to the M1, M4 applies the MPDioU loss function to the M1; M5 applies both the ODConv module and MPDioU loss function to the M1; M6 applies both the ODConv and DyHead modules to the M1; M7 applies both the DyHead module and MPDioU loss function to the M1; and M8 applies the ODConv and DyHead modules, and MPDioU loss function to the M1. The results, as shown in Table 7, indicate that the ODConv module enhanced detection accuracy, albeit at the cost of a slight decrease in mAP@0.5. The attention mechanism of the DyHead module improved the ability to extract important target features, resulting in a 4.4 % increase in mAP@0.5, as well as improvements in precision and recall. Compared with the YOLOv8 basic model, the improved YOLOv8 by replacing with the ODConv module, adding the DyHead module, and incorporating the MPDioU loss function enhanced the feature fusion capabilities and significantly improved global feature information extraction. The precision, recall, and mAP@0.5 performance improved to 91 %, 93 %, and 90.5 %, respectively, validating the effectiveness of the improved model.

Table 6
Comparison of experimental results of different models.

Model	Dataset	Precision	Recall	mAP@0.5
Faster RCNN	Dataset 1	0.801	0.72	0.67
	Dataset 2	0.851	0.81	0.84
	Dataset 3	0.882	0.87	0.882
	Dataset 4	0.89	0.88	0.9
YOLOv8 Basic	Dataset 1	0.83	0.82	0.77
	Dataset 2	0.82	0.82	0.91
	Dataset 3	0.85	0.87	0.82
	Dataset 4	0.87	0.88	0.835
YOLOv7	Dataset 1	0.65	0.67	0.63
	Dataset 2	0.68	0.69	0.68
	Dataset 3	0.72	0.7	0.69
	Dataset 4	0.78	0.73	0.71
Improved YOLOv8	Dataset 1	0.83	0.82	0.77
	Dataset 2	0.82	0.82	0.78
	Dataset 3	0.869	0.931	0.836
	Dataset 4	0.90	0.931	0.891

From Figs. 12 and 13, with an increase in the number of iterations, the improved YOLOv8 model exhibited the best mAP@0.5 performance across different datasets, and the model converged the fastest. In Dataset 4, the ablation experiments demonstrated that the improved YOLOv8 model achieved faster convergence, smaller convergence fluctuations, and better performance. Therefore, the results indicate that multispectral imagery can effectively identify PWD-diseased trees in complex environments. The improved YOLOv8 model exhibited significant advantages in terms of detection accuracy, scale, and speed.

It is worth noting that although this adjustment is effective in certain instances, it does not always achieve optimal results. An important factor to consider is that the addition of new attention modules increases the complexity of the calculations, which may not be the best choice for certain situations. Additional improvements can be made based on specific requirements. Future research could delve deeper into the YOLOv8 architecture to customize it according to specific application requirements, providing additional possibilities for further optimization and enhancing model performance in various scenarios.

It should also be noted that, in our sample dataset, there was a clear distinction between background objects and infected trees. We categorized the infected trees into fully and partially discolored, which allowed the model to better classify infected and uninfected trees. However, this also indicates that the distinction between mid- and late-stage infected trees is unclear. Therefore, effective differentiation between mid- and late-stage infected trees has become a challenge in the development of models for detecting PWD-infected trees in future research.

The identification results of the proposed and comparative models in practical applications are shown in Fig. 14, which displays the detection results of the different models on the validation set of the NDRE group dataset. (a), (b), (c), and (d) represent withered (W) and suspected withered trees (SW), respectively, enclosed in red boxes and labeled. A comparative analysis of the identification results indicates that the confidence scores of the improved YOLOv8 were all >0.5, which allows for more accurate identification and localization of individual PWD trees compared with other deep learning models. The positions of withered trees can be confirmed, whereas the confidence scores of suspected withered trees are <50 %, requiring manual verification of the disease occurrence.

An increasing number of researchers have begun to use deep learning models (Singh et al., 2018; Mohanty et al., 2016; Liu et al., 2022). For example, Qin et al. (2023) improved the YOLOv5 algorithm by optimizing multiple modules in its architecture, thereby achieving fast and accurate recognition of PWD-infected pine trees. However, the YOLOv8 model used in this study has higher detection accuracy, faster inference speed, an anchor-free mechanism, optimized loss functions, and greater flexibility and scalability than the YOLOv5 model. By improving the basic YOLOv8 model, both detection speed and accuracy were further optimized. Wang et al. (2012) designed an automatic detection framework based on satellite image data and a multiscale attention-UNet model that effectively improved the efficiency and accuracy of PWD detection, achieving a recall rate of 57.38 %. This study used UAV multispectral data. The advantage of using the improved YOLOv8 model lies in its high accuracy and fast detection capability after model improvement according to Table 8. It is suitable for the rapid and precise screening of epidemic areas, particularly in scenarios requiring high-precision detection and quick responses, with a detection accuracy >80 %. In addition, the UAV images used to create the dataset in this experiment represented a more severe stage of PWD infection, making it difficult to accurately identify PWD-infected trees in the early stages.

Table 7
Experimental results of different improvement ablation experiments on the optimal model.

Model	Label	ODConv	DyHead	MPDioU	Precision	Recall	mAP@0.5
Improved YOLOv8	M1				0.872	0.88	0.851
	M2	√			0.88	0.885	0.877
	M3		√		0.872	0.89	0.855
	M4			√	0.877	0.882	0.853
	M5	√		√	0.886	0.89	0.862
	M6	√	√		0.894	0.912	0.889
	M7		√	√	0.879	0.893	0.861
	M8	√	√	√	0.90	0.93	0.891

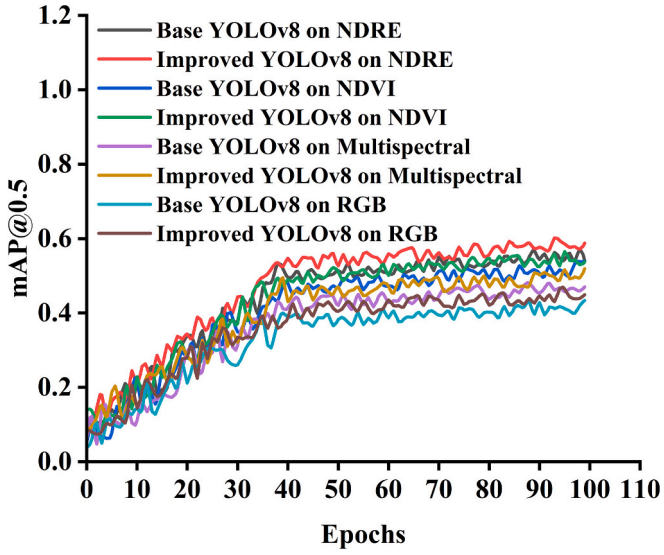


Fig. 12. Comparison of mAP@0.5 across different datasets.

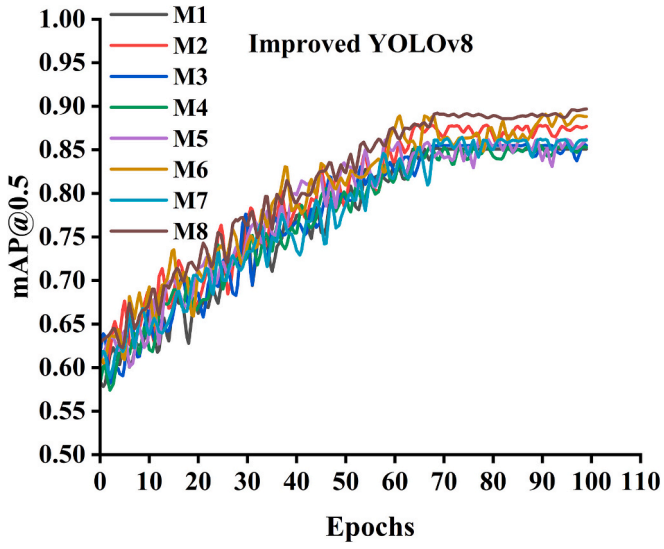


Fig. 13. Comparison of mAP@0.5 across different ablation experiments.

The limited number of samples of different ground objects in the images, such as red broadleaved trees, and early- and mid-stage infected pines, also affected the experimental results. In future research, efforts should be made to increase the number of sample images of various ground objects in model training to improve model classification and recognition accuracy.

4. Conclusions and future work

Rapid identification of PWD-infected trees is crucial for PWD prevention and control. However, owing to the influence of complex environments, identification models based on visible light or multispectral imaging datasets may experience omissions and false detections. This study found that in UAV multispectral images, the most sensitive band sequence for PWD-infected tree detection was red-edge band II, followed by NIR, red-edge I, G, and R bands, with the least sensitivity in the B band. That is, apart from the B band vegetation index, other vegetation indices have strong discriminative power for PWD-infected trees. This study used sensitive bands for PWD-infected trees and vegetation indices with strong discriminative power for PWD-infected trees to construct four sets of data as training datasets. Different deep learning models were compared in terms of recognition accuracy and model runtime. By adopting the feature extraction ODConv and attention mechanism DyHead modules, the features of PWD-infected trees were more accurately captured. The MPDioU loss function was applied to predict low-redundancy results, improve the regression accuracy and model runtime efficiency, and construct the optimal deep learning model YOLOv8. The improved YOLOv8 model achieved an mAP@0.5 of 89.1 %, user accuracy of 90 %, and a recall rate of 93.1 %, fully demonstrating the effectiveness of the model. This model is expected to provide rapid and accurate detection of PWD-infected trees in complex environments.

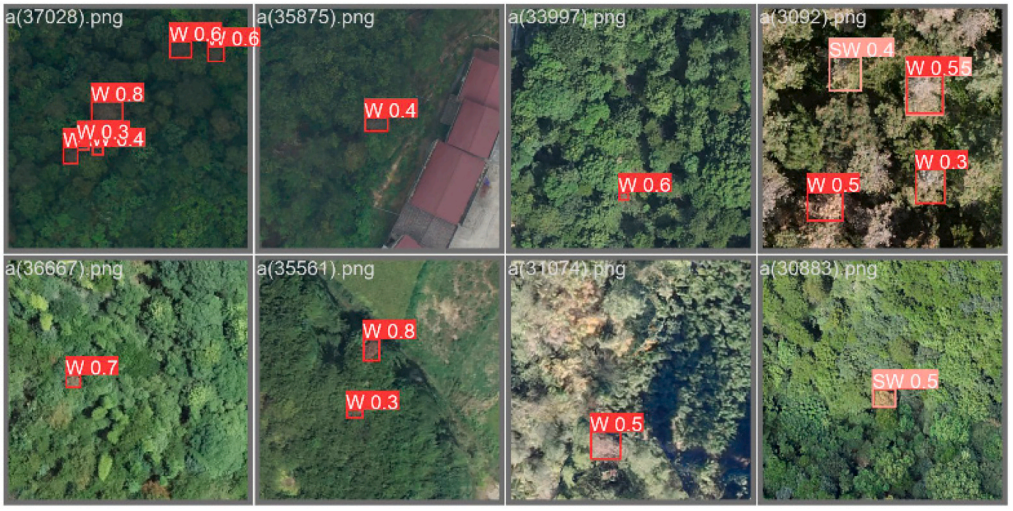
Rapid identification is crucial for the prevention and control of PWD-infected trees. However, owing to the influence of complex environments, detection models based on visible light or multispectral imaging datasets may result in false-negatives and -positives. We constructed a sample dataset of PWD-infected trees, containing 6050 preprocessed images. In the drone imagery used in this study, the diameter of the tree crowns was $<600 \times 600$ pixels, therefore, 1280×960-pixel images were cropped to 600×600 pixels, beginning from the center of the existing images. After data segmentation, 8560 images were used for training, 1070 for validation, and 985 for testing.

This study analyzed the spectral characteristics and physiological vegetation parameters of healthy, PWD-infected fully discolored, and partially discolored pine trees. These results suggest that the observed pattern of needle reflectance may be due to the significant influence of chlorophyll on plant spectral reflectance within the 400–700 nm wavelength range. As the needles transitioned from healthy to discolored and dead, the chlorophyll content in the needles gradually decreased, reducing the absorption effect of chlorophyll and thereby increasing reflectance. In the 700–1300 nm wavelength range, reflectance began to increase rapidly at approximately 700 nm, exhibiting the "red-edge" phenomenon characteristic of vegetation spectra. In the 1300–2500 nm wavelength range, the spectral reflectance of vegetation is related to the leaf water content, with reduced needle water content leading to a significant increase in reflectance.

In this experiment, the spectral curve of healthy pine needles was used as the baseline, and the relative distances between the spectral curves of the fully discolored, partially discolored, and healthy pine trees were calculated using the Euclidean distance formula. The results showed that the red-edge band II (750 nm) was the most sensitive for distinguishing between healthy needles and those with two different



（a）



（b）



（c）

Fig. 14. Identification results: (a) Faster R-CNN, (b) YOLOv7, (c) improved YOLOv8, and (d) YOLOv8 basic models.



(d)

Fig. 14. (*continued*).

Table 8
Recognition accuracy analysis of different models on the prediction dataset.

Model	Style	Correct identifications (trees)	Number of identifications (trees)	Correctly identified (trees)	False positive identifications (trees)	Missed detections (trees)	Precision (%)	Recall (%)	mAP@0.5 (%)
Faster RCNN	SW	85	62	43	19	42	69.35 %	50.59 %	68.57 %
	W	101	78	60	18	41	76.92 %	59.41 %	68.34 %
YOLOv7	SW	85	56	41	15	44	73.21 %	48.24 %	60.72 %
	W	101	62	48	14	53	77.42 %	47.52 %	62.43 %
YOLOv8 basic	SW	85	69	51	18	34	73.91 %	60.00 %	68.32 %
	W	101	73	58	15	43	79.45 %	57.43 %	67.53 %
Improved YOLOv8	SW	85	76	55	11	20	73.68 %	65.88 %	62.28 %
	W	101	88	76	12	25	86.36 %	75.25 %	89.10 %

degrees of discoloration and death, followed by the NIR (840 nm), red-edge I (720 nm), G (555 nm), and R (660 nm) bands, with the B band being the least sensitive.

To further improve the accuracy of the base YOLOv8 model for identifying PWD-infected trees, we used bands containing PWD-sensitive wavelengths and PWD-distinguishable vegetation indices to form four groups of data as training datasets. The accuracy and speed of different deep learning models were compared. By incorporating the ODConv module for feature extraction and the DyHead module for attention mechanisms, the features of PWD-infected trees were more accurately captured. The MPDioU loss function was applied to predict the results with low redundancy, thereby improving regression accuracy and model efficiency. This led to the development of an optimized deep learning model, an improved version of YOLOv8. The mAP@0.5 of the improved YOLOv8 model increased to 89.1 % with a user accuracy of 90 % and a recall rate of 93.1 %, fully demonstrating the effectiveness of the model. This model shows promise for the rapid and accurate detection of PWD-infected trees in complex environments.

Despite these improvements, there remain some limitations in detecting PWD-infected trees in real-world monitoring scenarios using the YOLOv8 model. The image acquisition environment can affect the image quality, and blurred or unclear image features can reduce the detection accuracy (Syifa et al., 2020; Qin et al., 2021). In addition, changes in pine tree crown color caused by drought and other pests can affect the detection of infected trees (Hu et al., 2020). Therefore, to minimize the interference of environmental factors on detection accuracy, it is necessary to avoid excessive direct sunlight and overcast conditions during drone data collection and to clearly identify pathogenic agents in the monitored forest areas.

Moreover, the accuracy of PWD-infected tree detection is improved by increasing the number of model parameters and replacing the detection modules; however, this sacrifices some detection speed. Models such as Faster R-CNN, YOLOv7, and the base version of YOLOv8 have fewer model parameters, resulting in lower detection accuracy for PWD-infected trees but reduced deployment costs, making them suitable for detecting infected pine trees on mobile devices. Conversely, the improved YOLOv8 model with its slower detection speed and higher detection accuracy is more suitable for deployment on laptops or cloud servers. Therefore, different automatic recognition models can be deployed based on the specific detection devices.

In future studies, we plan to categorize hyperspectral data from early infected pines based on different appearances and identify various pine diseases. In addition, we intend to design a lightweight detection network to better balance accuracy and speed, thereby further adapting to different devices for detecting PWD-infected trees with varying degrees of infection.

Funding

This research was funded by the National Key Research and Development Program of China (2021YFD1400900); National Natural Science Foundation of China (42201355); Supported by Hainan Provincial Natural Science Foundation of China (322QN346), CNR-CAS project: Research on Remote Sensing Monitoring of Crop Growth and Disease and Pest under the Background of Climate Change.

CRediT authorship contribution statement

Shaoxiong Xu: Writing – original draft, Software, Data curation, Conceptualization. **Wenjiang Huang:** Writing – review & editing, Resources, Methodology, Funding acquisition. **Dacheng Wang:** Project administration. **Biyao Zhang:** Writing – original draft, Supervision. **Hong Sun:** Methodology, Investigation. **Jiayu Yan:** Methodology. **Jianli Ding:** Supervision. **Jinjie Wang:** Validation. **Qiuli Yang:** Data curation. **Tiecheng Huang:** Data curation. **Xu Ma:** Investigation. **Longlong Zhao:** Validation, Investigation. **Zhuoqun Du:** Writing – review & editing.

Declaration of competing interest

The authors declare that they have no known competing financial interests or personal relationships that could have appeared to influence the work reported in this paper.

Data availability

The PWD UAV Multispectral Imagery dataset and software program in this study are publicly available at https://doi.org/10.17632/3cf7t4xvw6.1.

Acknowledgments

The authors gratefully acknowledge YUSENSE for providing the software. We thank Ke Zhang for help with the fieldwork. In addition, Shaoxiong Xu would like to thank Shaohua Xu for the help in typesetting. We would like to thank the reviewers for their helpful and constructive comments, which have improved the paper.

References

Abelleira, A., Picoaga, A., Mansilla, J.P., Aguin, O., 2011. Detection of Bursaphelenchus xylophilus, causal agent of pine wilt disease on Pinus pinaster in northwestern Spain. Plant Dis. 95 (776). https://doi.org/10.1094/PDIS-12-10-0902.

Aoden, Yang Jiahui, Weiting, Ding, et al., 2023. A review of research progress on 54 vegetation indices [J]. Anhui Agric. Sci. 51 (1), 13–21, 28. https://doi.org/10.3969/j.issn.0517-6611.2023.01.004.

Apan, A., Held, A., Phinn, S., Markley, J., 2004. Detecting sugarcane 'orange rust' disease using EO-1 Hyperion hyperspectral imagery. Int. J. Remote Sens. 25 (2), 489–498. https://doi.org/10.1080/01431160310001618086.

Awad, M.M., 2018. Forest mapping: a comparison between hyperspectral and multispectral images and technologies. J. For. Res. 29 (5), 1395–1405. https://doi.org/10.1007/s11676-017-0528-y.

Bochkovskiy, A., Wang, C.Y., Liao, H.Y.M., 2004. YOLOv4:Optimal Speed and Accuracy of Object Detection. arXiv 2020,arXiv:2004.10934. https://arxiv.org/abs/2004.10934.

Dai, X.Y., Chen, Y.P., Xiao, B., Chen, D.D., Liu, M.C., Yuan, L., Zhang, L., 2021. Dynamic head: unifying object 510 detection heads with attentions. In: Proceedings of the IEEE/CVF Conference on Computer Vision and Pattern 511 Recognition, pp. 7373–7382. https://doi.org/10.48550/arXiv.2106.08322.

de Melo Lima, B.P., Borges, L.D.A.B., Hirose, E., Borges, D.L., 2024. A lightweight and enhanced model for detecting the Neotropical brown stink bug, Euschistus heros (Hemiptera: Pentatomidae) based on YOLOv8 for soybean fields. Eco. Inform. 80, 102543. https://doi.org/10.1016/j.ecoinf.2024.102543.

Deng, B., Lu, Y., Xu, J., 2024. Weed database development: an updated survey of public weed datasets and cross-season weed detection adaptation. Eco. Inform. 81, 102546. https://doi.org/10.1016/j.ecoinf.2024.102546.

Doe, J., Smith, A., Zhang, B., 2023. YOLOv8: Advanced Convolutional Architectures and Attention Mechanisms for Enhanced Speed and Robustness arXiv preprint arXiv: 2301.12345. https://arxiv.org /abs/2301.12345.

Dong, C., Zhao, G., Meng, Y., Li, B., Peng, B., 2020a. The effect of topographic correction on forest tree species classification accuracy. Remote Sens. 12 (5), 787. https://doi.org/10.3390/rs12050787.

Dong, C., Zhao, G., Meng, Y., Li, B., Peng, B., 2020b. The effect of topographic correction on forest tree species classification accuracy. Remote Sens. 12 (5), 787. https://doi.org/10.3390/rs12050787.

Eugenio, F.C., Pereirada Silva, S.D., Fantinel, R.A., de Souza, P.D., Felippe, B.M., Romua, C.L., Elsenbach, E.M., 2021. Remotely piloted aircraft systems to identify pests and diseases in forest species: the global state of the art and future challenges. IEEE Geosci. Remote Sens. Mag. https://doi.org/10.1109/MGRS.2021.3087445.

Franke, J., Menz, G., 2007. Multi-temporal wheat disease detection by multi-spectral remote sensing. Precis. Agric. 8, 161–172. https://doi.org/10.1007/s11119-007-9036-y.

Futai, K., 2013. Pine wood nematode, Bursaphelenchus xylophilus. Annu. Rev. Phytopathol. 51, 61–83. https://doi.org/10.1146/annurev-phyto-081211-172910.

Ge, Z., Liu, S., Wang, F., Li, Z., Sun, J., 2021. Yolox: Exceeding Yolo Series in 2021. arXiv 2021, arXiv:2107.08430. https://doi.org/10.48550/arXiv.2107.08430.

Gitelson, A.A., Kaufman, Y.J., Merzlyak, M.N., 1996. Use of a Green Channel in remote sensing of global vegetation from EOS-MODIS. Remote Sens. Environ. 58 (3), 289–298. https://doi.org/10.1016/S0034-4257(96)00072-7.

Gruffudd, H.R., Schröder, T., Jenkins, T.A.R., et al., 2019. Modelling pine wilt disease (PWD) for current and future climate scenarios as part of a pest risk analysis for pine wood nematode Bursaphelenchus xylophilus (Steiner and Buhrer) Nickle in Germany. J. Plant Dis. Prot. 126, 129–144. https://doi.org/10.1007/s41348-018-0197-x.

Han, Y., Zhang, Y.H., Chen, Z.Q., Zhu, R.F., Yan, Z.Y., 2021. A study on the grassland quality evaluation method based on red-edge bands. J. Jilin Univ. (Inform. Sci. Ed.) 39 (02), 178–184. https://doi.org/10.19292/j.cnki.jdxxp.2021.02.008.

Hu, G., Yin, C., Wan, M., Zhang, Y., Fang, Y., 2020. Recognition of diseased Pinus trees in UAV images using deep learning and AdaBoost classifier. Biosyst. Eng. 194, 138–151. https://doi.org/10.1016/j.biosystemseng.2020. 03.021.

Iordache, M.D., Mantas, V., Baltazar, E., Pauly, K., Lewyckyj, N., 2020. A machine learning approach to detecting pine wilt disease using airborne spectral imagery. Remote Sens. 12, 2280. https://doi.org/10.3390/rs12142280.

Istiak, M.A., Syeed, M.M., Hossain, M.S., Uddin, M.F., Hasan, M., Khan, R.H., Azad, N.S., 2023. Adoption of unmanned aerial vehicle (UAV) imagery in agricultural management: a systematic literature review. Eco. Inform. 102305. https://doi.org/10.1016/j.ecoinf.2023.102305.

Jordan, C.F., 1969. Derivation of leaf-area index from quality of light on the forest floor. Ecology 50 (4), 663–666. https://doi.org/10.2307/1936256.

Kim, D.S., et al., 2009. Escape of pine wood nematode, Bursaphelenchus xylophilus, through feeding and oviposition behavior of Monochamus alternatus and M. saltuarius (Coleoptera: Cerambycidae) adults. Korean. J. Appl. Entomol. 48 (4), 527–533. https://doi.org/10.5656/KSAE.2009.48.4.527.

Kim, S.R., Lee, W.K., Lim, C.H., Kim, M., Kafatos, M.C., Lee, S.H., Lee, S.S., 2018. Hyperspectral analysis of pine wilt disease to determine an optimal detection index. Forests 9 (115). https://doi.org/10.3390/f9030115.

Lee, D.S., Choi, W.I., Nam, Y., Park, Y.S., 2021. Predicting potential occurrence of pine wilt disease based on environmental factors in South Korea using machine learning algorithms. Eco. Inform. 64, 101378. https://doi.org/10.1016/j.ecoinf.2021.101378.

Li, C., Zhou, A., Yao, A., 2022. Omni-dimensional dynamic convolution. arXiv preprint arXiv:2209.07947. https://doi.org/10.48550/arXiv.2209.07947.

Li, L., Xin, X., Zhao, J., et al., 2023. Remote sensing monitoring and assessment of global vegetation status and changes during 2016-2020. Sensors (Basel, Switzerland) 23 (20), 8452. https://doi.org/10.3390/s23208452.

Liu, X., Zhang, S., Yang, B., 2020. Deep learning approaches for disease detection in trees using high-resolution aerial imagery. J. Plant Pathol. 102 (4), 823–833. https://doi.org/10.1007/s42161 -019-00412-2.

Liu, L., Zheng, X.M., Jiang, T., et al., 2021. A review of extraction methods for vegetation coverage using UAV remote sensing. J. Northeast Norm. Univ. (Nat. Sci. Ed.) 53 (04), 151–160. https://doi.org/10.16163/j.cnki.22-1123/n.2021.04.023.

Liu, S.C., Wang, Q., Tang, Q., Liu, L., He, H.Y., Lu, J.F., Dai, X.Q., 2022. High-resolution imagery identification of trees with pinewood nematode disease based on multi-feature extraction and deep learning with attention mechanism. J. Forest. Eng. 7, 177–184. https://doi.org/10.13360/j.issn.2096-1359.202011015.

Lou, H., Duan, X., Guo, J., Liu, H., Gu, J., Bi, L., Chen, H., 2023. DC-YOLOv8: small-size object detection algorithm based on camera sensor. Electronics 12 (10), 2323. https://doi.org/10.3390/electronics12102323.

Ma, N., Hu, Y.F., Zhuang, D.F., Wang, X.S., 2010. Determination on the optimum band combination of HJ-1A hyperspectral data in the case region of Dongguan based on optimum index factor and J-M distance. Remote Sens. Technol. Appl. 25 (03), 358–365. https://doi.org/10.11873/j.issn.1004-0323.2010.3.358.

Mohanty, S.P., Hughes, D.P., Salathé, M., 2016. Using deep learning for image-based plant disease detection. Front. Plant Sci. 7, 1419. https://doi.org/10.3389/fpls.2016.01419.

Oide, A.H., Nagasaka, Y., Tanaka, K., 2022. Performance of machine learning algorithms for detecting pine wilt disease infection using visible color imagery by UAV remote sensing. Remote Sens. Appl. 28, 100869. https://doi.org/10.1016/j.rsase.2022.100869.

Park, Y.S., Chung, Y.J., Moon, Y.S., 2013. Hazard ratings of pine forests to a pine wilt disease at two spatial scales (individual trees and stands) using self-organizing map and random forest. Eco. Inform. 13, 40–46. https://doi.org/10.1016/j.ecoinf.2012.10. 008.

Park, H.G., Yun, J.P., Kim, M.Y., Jeong, S.H., 2021. Multichannel object detection for detecting suspected trees with pine wilt disease using multispectral drone imagery. IEEE J. Sel. Top. Appl. Earth Obs. Remote Sens. 14, 8350–8358. https://doi.org/10.1109/JSTARS. 2021.3118544.

Pearson, R.L., 1972. Remote mapping of standing crop biomass for estimation of the productivity of the short-grass prairie, Pawnee National Grasslands, Colorado. Ecology 45 (2), 7–12. https://doi.org/10.2307/1935414.

Pu, R., Gong, P., 2019. Hyperspectral remote sensing of forest health: monitoring the impacts of environmental stress on forest canopies. J. Environ. Manag. 231, 85–97. https://doi.org/10.1016/j.jenvman.2018.12.013.

Qin, J., Wang, B., Wu, Y., Lu, Q., Zhu, H., 2021. Identifying pine wood nematode disease using UAV imagery and deep learning algorithms. Remote Sens. 13, 162. https://doi.org/10.3390/rs13020162.

Qin, Bingxi, Sun, Fenggang, Shen, Weixing, Dong, Bin, Ma, Shencheng, Huo, Xinyu, Lan, Peng, 2023. Deep learning-based pine nematode Trees' identification using

multispectral and visible UAV imagery. Drones 7 (3), 183. https://doi.org/10.3390/drones7030183.
Rani, S.J., Ioannou, I., Swetha, R., Lakshmi, R.D., Vassiliou, V., 2024. A novel automated approach for fish biomass estimation in turbid environments through deep learning, object detection, and regression. Eco. Inform. 102663. https://doi.org/10.1016/j.ecoinf. 2024.102663.
Ren, S., He, K., Girshick, R., Sun, J., 2015. Faster R-CNN: towards real-time object detection with region proposal networks. IEEE Trans. Pattern Anal. Mach. Intell. 39 (6), 1137–1149. https://doi.org/10.1109/TPAMI.2016.2577031.
Ren, D., Peng, Y., Sun, H., Yu, M., Yu, J., Liu, Z., 2022. A global multi-scale channel adaptation network for pine wilt disease tree detection on UAV imagery by circle sampling. Drones 6, 353. https://doi.org/10.3390/drones6110353.
Rencz, A.N., Nemeth, J., 1985. Detection of mountain pine beetle infestation using Landsat MSS and simulated thematic mapper data. Can. J. Remote. Sens. 11, 50–58. https://doi.org/10.1080/07038992.1985.10855077.
Riley, J.R., 1989. Remote sensing in entomology. Annu. Rev. Entomol. 34 (1), 247–271. https://doi.org/10.1146/annurev.en.34.010189.001335.
Rohit, Sharma, Verma, Singh, Dr Sourabh, Dhaka, Singh, Dr Vijaypal, 2024. SAR images change detection using proposed lamina attention-based noise-resistant UNet advance network (LANRUNet++). Digit. Sign. Process. 155, 104726. https://doi.org/10.1016/j.dsp.2024.104726.
Rutherford, T.A., Mamiya, Y., Webster, J.W., 1990. Nematode-induced pine wilt disease: factors influencing its occurrence and distribution. For. Sci. 36 (1), 145–155. https://doi.org/10.1093/forestscience/ 36.1.145.
Singh, A., Ganapathysubramanian, B., Singh, A.K., Sarkar, S., 2018. Machine learning for high-throughput stress phenotyping in plants. Trends Plant Sci. 23 (9), 798–811. https://doi.org/10.1016/j.tplants.2018.07.004.
Smith, J.A., Johnson, K.R., Wang, L., Gupta, A., Hernandez, M.T., Zhao, H., 2021. Remote sensing for early detection of forest disease using multispectral imaging. Sensors 21, 876. https://doi.org/10.3390/s21030876.
Sunil, G.C., Upadhyay, Arjun, Zhang, Yu, Howatt, Kirk, Peters, Thomas, Ostlie, Michael, et al., 2024. Field-based multispecies weed and crop detection using ground robots and advanced YOLO models: A data and model-centric approach. Smart Agric. Technol. 9, 100538. https://doi.org/10.1016/j.atech.2024.100538.
Syifa, M., Park, S.-J., Lee, C.-W., 2020. Detection of the pine wilt disease tree candidates for drone remote sensing using artificial intelligence techniques. Engineering 2020 (6), 919–926. https://doi.org/10.1016/j. eng.2020. 07.001.
Tang, S.H., Zhu, Q.J., Wang, J.D., et al., 2003. Theoretical basis and application of the three-band gradient difference vegetation index. Sci. China Ser. D Earth Sci. 33 (11), 1094–1102. https://doi.org/10.1360/02yd0527.
Tao, H., Li, C., Zhao, D., Deng, S., Hu, H., Xu, X., Jing, W., 2020. Deep learning-based dead pine tree detection from unmanned aerial vehicle imagery. Int. J. Remote Sens. 41, 8238–8255. https://doi.org/10.1080/01431161.2020.1766145.
Tian, Q.J., 1998. Advances in research on vegetation indices. Adv. Earth Science 13 (4), 327–333. https://doi.org/10.11867/j.issn.1001-8166.1998.04.0327.
Verrelst, J., Schaepman, M.E., Koetz, B., et al., 2008. Angular sensitivity analysis of vegetation indices derived from CHRIS/PROBA data. Remote Sens. Environ. 112 (5), 2341–2353. https://doi.org/10.1016/j.rse.2007.11.001.
Vollenweider, P., Günthardt-Goerg, M.S., 2006. Diagnosis of abiotic and biotic stress factors using the visible symptoms in foliage. Environ. Pollut. 140, 562–571. https://doi.org/10.1016/j.envpol.2005.01.032.
Wang, L.G., Tian, Y.C., Li, W.L., et al., 2012. Estimation of nitrogen accumulation in winter wheat leaves based on ground-air remote sensing coupling. Chin. J. Appl. Ecol. 23 (1), 73–80. https://doi.org/10.1109/Agro-Geoinformatics59224.2023.10233310.
Wang, C.Y., Bochkovskiy, A., Liao, H.-Y.M., 2022a. YOLOv7: trainable bag-of-freebies sets new state-of-the-art for real-time object detectors arXiv preprint arXiv: 2207.02696. https://arxiv.org/abs/2207.02696.
Wang, J., Zhao, J., Sun, H., Lu, X., Huang, J., Wang, S., Fang, G., 2022b. Satellite remote sensing identification of discolored standing trees for pine wilt disease based on semi-supervised deep learning. Remote Sens. 2022 (14), 5936. https://doi.org/10.3390/rs14235936.
Xiao, Deqin, Wang, Handong, Liu, Youfu, Li, Wengang, Li, Hongbin, 2024. DHSW-YOLO: a duck flock daily behavior recognition model adaptable to bright and dark conditions. Comput. Electron. Agric. 225, 109281. https://doi.org/10.1016/j.compag.2024.109281.
Xue, J.R., Su, B.F., 2017. Significant remote sensing vegetation indices: a review of developments and applications. J. Sens. 2017, 1–17. https://doi.org/10.1155/2017/1353691.
Xue, Y., Ju, Z., Li, Y., et al., 2021. MAF-YOLO:Multi-modal attention fusion based YOLO for pedestrian detection. Infrared Phys. Technol. 118, 103906. https://doi.org/10.1016/j.infrared.2021.103906.
Yahyanejad, S., Misiorny, J., Rinner, B., 2011. Lens distortion correction for thermal cameras to improve aerial imaging with small-scale UAVs. In: Proc. IEEE Int. Symp. Robot. Sensors Environ, 2011, pp. 231–236. https://doi.org/10.1109/ROSE.2011.6058528.
Yang, Sw, Dong, B., Liu, L., et al., 2015. Research on vegetation coverage change in sheng Jin Lake wetland of Anhui Province. Wetlands 35, 677–682. https://doi.org/10.1007/s13157-015-0657-z.
Ye, J.R., 2019. Epidemic status of pine wilt disease in China and its prevention and control techniques and countermeasures. Sci. Silvae Sin. 55 (9), 1–10. http://www.linyekexue.net/EN/10.11707/j.1001-7488.20190901.
Ye, W., Lao, J., Liu, Y., Chang, C.C., Zhang, Z., Li, H., Zhou, H., 2022. Pine pest detection using remote sensing satellite images combined with a multi-scale attention-UNet model. Eco. Inform. 72, 101906. https://doi.org/10.1016/j.ecoinf.2022.101906.
Yu, R., Luo, Y., Li, H., Yang, L., Huang, H., Yu, L., Ren, L., 2021. Three-dimensional convolutional neural network model for early detection of pine wilt disease using UAV-based hyperspectral images. Remote Sens. 13 (20), 4065. https://doi.org/10.3390/rs13204065.
Zeng, Y., Hao, D., Huete, A., et al., 2022. (2022). Optical vegetation indices for monitoring terrestrial ecosystems globally. Nat. Rev. Earth Environ. 3, 477–493. https://doi.org/10.1038/s43017-022-00298-5.
Zhang, Tao, Guan, Haiou, Ma, Xiaodan, Shen, Panpan, 2023. Drought recognition based on feature extraction of multispectral images for the soybean canopy. Ecol. Inform. 77 (102248), 1574–9541. https://doi.org/10.1016/j.ecoinf.2023.102248.
Zhenzuo, Zhang, Li, Jiawei, Cuiwen, Su, Wang, Zhiyong, Li, Yachao, Li, Daoliang, et al., 2024. A method for counting fish based on improved YOLOv8. Aquac. Eng. 107, 102450. https://doi.org/10.1016/j.aquaeng.2024.102450.
Zhou, H., Kong, M., Yuan, H., Pan, Y., Wang, X., Chen, R., Yang, Q., 2024. Real-time underwater object detection technology for complex underwater environments based on deep learning. Eco. Inform. 102680. https://doi.org/10.1016/j.ecoinf.2024. 102680.
Zong, S.X., Bi, H.J., 2022. Monitoring progress and prospect of pine wilt disease based on UAV remote sensing. Forest Pest Dis. 41, 45–51. https://doi.org/10.19688/j.cnki.issn1671-0886.20220037.